

AD-A240 982

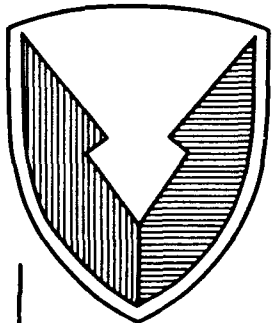


(2)



RD&E

CENTER



Technical Report

No. 13533

THERMAL WAVE IMAGING

EXAMPLES AND APPLICATIONS

JUNE 1991

DTIC
SELECTED
SEP 25 1991

S D

91-11386



D. H. Rose, D. C. Bryk, G. H. Guay,
W. D. Jackson, M. Parnes, J. A. Siwicki,
J. C. Moulder, D. J. Snoha, C. O. Ruud
and J. Dumar

ATTN: AMSTA-RSA
By Warren, MI 48397-5000

APPROVED FOR PUBLIC RELEASE:
DISTRIBUTION IS UNLIMITED

9 1 9 24 041

U.S. ARMY TANK-AUTOMOTIVE COMMAND
RESEARCH, DEVELOPMENT & ENGINEERING CENTER
Warren, Michigan 48397-5000

NOTICES

This report is not to be construed as an official Department of the Army position.

Mention of any trade names or manufacturers in this report shall not be construed as an official endorsement or approval of such products or companies by the U.S. Government.

Destroy this report when it is no longer needed. Do not return it to the originator.

REPORT DOCUMENTATION PAGE

Form Approved
OMB No. 0704-0188

The reporting burden for this collection of information is estimated to average 1 hour per response, including the time for reviewing instructions, searching existing data sources, gathering and maintaining the data needed, and completing and reviewing the collection of information. Send comments regarding this burden estimate or any other aspect of this collection of information, including suggestions for reducing the burden, to Washington Headquarters Service, Directorate for Information Operations and Reports, 1215 Jefferson Davis Highway, Suite 1204, Arlington, VA 22202-4302, and to the Office of Management and Budget, Paperwork Reduction Project (0704-0188), Washington, DC 20503.

1. AGENCY USE ONLY (Leave Blank)	2. REPORT DATE	3. REPORT TYPE AND DATES COVERED
	Jun 91	Interim: 1980-90
4. TITLE AND SUBTITLE		5. FUNDING NUMBERS
Thermal Wave Imaging Examples and Applications		
6. AUTHOR(S) D.N. Rose, D.C. Bryk, G.H. Quay, W.D. Jackson, M. Parnes, J.A. Siwicki, J.C. Moulder, D.J. Snoha, C.O. Ruud and J. Dumat		8. PERFORMING ORGANIZATION REPORT NUMBER
7. PERFORMING ORGANIZATION NAME(S) AND ADDRESS(ES) Applied Research Branch (AMSTA-RSA) Research, Development and Engineering Center U.S. Army Tank-Automotive Command Warren, MI 48397-5000		13533
9. SPONSORING/MONITORING AGENCY NAME(S) AND ADDRESS(ES)		10. SPONSORING/MONITORING AGENCY REPORT NUMBER
11. SUPPLEMENTARY NOTES		
12a. DISTRIBUTION/AVAILABILITY STATEMENT Approved for Public Release Distribution Unlimited		12b. DISTRIBUTION CODE
13. ABSTRACT (Maximum 200 words)		
<p>This is a brief introduction to the thermal wave principle with illustrations from ongoing work performed in connection with the photoacoustic microscopy laboratory at the U.S. Army Tank-Automotive Command.</p> <p>The photoacoustic or thermal wave technique offers a unique path for evaluation of the surface and near surface thermal properties and structure of a material. An example of one micron surface resolution will demonstrate the detail available. The variety of detection approaches will be illustrated with gas-cell images; photoinductive images showing resolution 15 times better than achieved before with an eddy current imaging approach; and an image generated by an ion beam in which piezoelectric detection was used. The potential for quantifying the thickness and thermal properties of coatings will be demonstrated. Work in progress relating gas-cell images obtained with high laser intensity, which intentionally modified the surface, to subsequent x-ray measurement of residual stress will be presented.</p>		
14. SUBJECT TERMS		15. NUMBER OF PAGES 31
Photoacoustic microscopy, thermal wave imaging, x-ray residual stress determination, photoinductive detection, chemical vapor deposited silicon carbide		16. PRICE CODE
17. SECURITY CLASSIFICATION OF REPORT UNCLASSIFIED	18. SECURITY CLASSIFICATION OF THIS PAGE UNCLASSIFIED	19. SECURITY CLASSIFICATION OF ABSTRACT UNCLASSIFIED
		20. LIMITATION OF ABSTRACT SAR

Contents

INTRODUCTION	1
Principle.....	1
Figure 1. Temperature-related effects from periodic heating.	2
Figure 2. Vertical milling roughness standard.	4
Figure 3. 45° slanted crack.	5
Figure 4. Ion acoustic macrograph.	6
Figure 5. Fatigue crack in aluminum imaged with both gas-cell and mirage detection.	7
Figure 6. Comparison of gas-cell and mirage detection of Knoop indentations on sintered SiC.	8
Figure 7. Resolution demonstration with eddy-current detection.	9
Figure 8. Photoinductive images of a thermal barrier coating.	10
Figure 9. Chemical vapor deposited SiC on graphite.	11
Figure 10. Images of the right-hand edge of the spalled region.	12
Figure 11. Images with 1 μm features.	13
Figure 12. A 1 X 1 mm area of Figure 9.	14
Figure 13. The area of Figure 12 at different modulation frequencies.	15
Figure 14. CVD SiC on sintered α SiC.	16
Figure 15. CVD SiC on sintered α SiC. The area of Figure 14 at 1 KHz.	17
Figure 16. Residual stress in CVD SiC sample 3B to 49-41 edge.	18
Figure 17. Residual stress in CVD SiC sample 3B \perp to 49-41 edge.	19
Figure 18. Overall scan of locations irradiated with high laser power.	20
Figure 19. Optical micrograph of corner of area irradiated with highest laser power.	21
Figure 20. Postlaser irradiation residual stress to 49-41 edge.	22
Figure 21. Postlaser irradiation residual stress \perp to 49-41 edge.	23

Summary	24
Acknowledgments	24
References	24
DISTRIBUTION LIST	27

87
2000-0000

Accession for	NTIC	DA	✓
DTIC	TSB		
Classification			
Justification			
By			
Distribution			
Serial Number			
Dist			
A-1			

INTRODUCTION

The photoacoustic effect was first reported by Alexander Graham Bell in 1880. Within a year, further investigations were carried out by the famous, including Bell and his associate Tainter, Roentgen (15 years before his discovery of x-rays) and Lord Rayleigh, as well as by the not-so-famous, such as Mercadier and also Preece, who came closest to our modern explanation of the effect. After a flurry of initial interest, the effect lay dormant for 50 years until improved microphones allowed quantification of the sound. At that time, Viengerov in the Soviet Union revived it for work with gases. However, it was not reapplied to solids until about 16 years ago. The first photoacoustic microscopy image presented as a graphical plot was produced only 12 years ago.

The advent of the laser and the development of modern signal processing techniques have made photoacoustics, also known as thermal wave imaging, a viable technique for nondestructive evaluation of various materials. Using it, the surface and near surface *thermal* properties of a material can be probed.

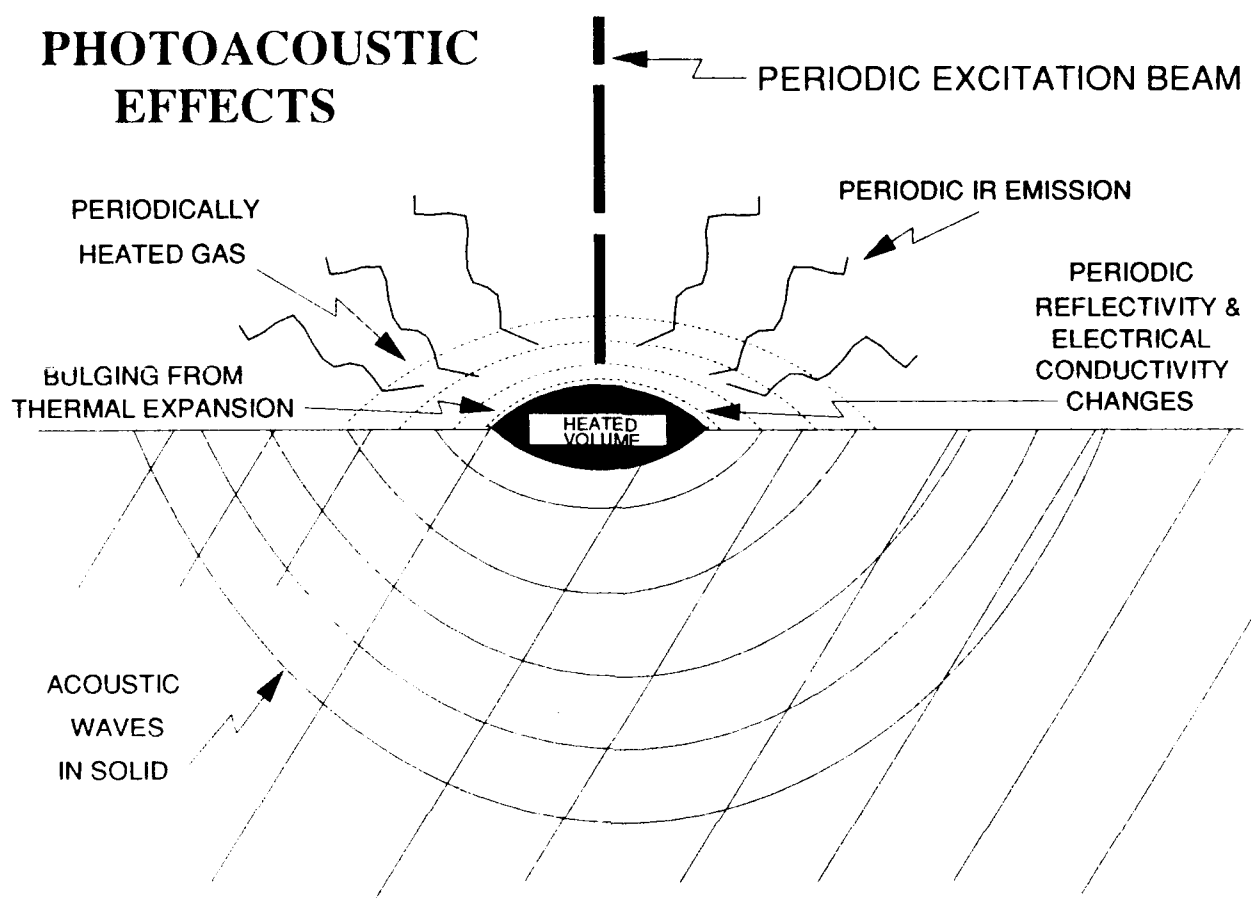
This report is intended as a brief introduction to the thermal wave principle with illustrations from actual thermal wave images and ongoing work performed in connection with the photoacoustic microscopy laboratory at the U.S. Army Tank-Automotive Command. A much more detailed introduction has been given before¹.

Principle

The first figure schematically illustrates some of the effects in solids from periodic or transient heating. A periodic excitation beam is incident on the surface causing a periodic temperature change. The temperature variation is detected through secondary effects. Bell's approach, which will be called "gas cell" here, was historically first. In this approach, an enclosed cell, which includes a window for the radiation to enter, is placed on the surface to be examined. The periodic temperature change on the surface causes periodic temperature changes in the air above the surface and, hence, periodic pressure changes in the closed cell which are detected using a microphone. Another approach, "optical beam deflection" or "mirage", samples the heated air by skimming a probe laser beam above the surface which is periodically deflected by the variations in the gradient of the index of refraction in the air above the periodically heated spot. A third approach to be illustrated here relies on the acoustic vibrations generated in the excited spot by the periodic expansion and contraction of the material. The vibrations are then detected by piezoelectric transducers affixed to the sample. Other detection modalities have been used to good effect. For example, a probe laser may be bounced off the shoulder of the heated spot and will then be periodically deflected by the bulging of the heated spot and, to some extent, the heated air above the spot. The reflectivity of most materials is a function of temperature which furnishes yet another route which has been applied particularly to semiconductor slices. The other detection scheme to be illustrated here, eddy current detection, relies on the change in electrical conductivity with temperature in the heated spot which is detected via an eddy current coil.

Figure 1. Temperature-related effects from periodic heating.

PHOTOACOUSTIC EFFECTS



Infrared (IR) detection merits special mention, though examples of it are not shown here. IR cameras are capable of noncontact whole field viewing and thus represent a major area of present work in the field. Newer ideas in the field of IR imaging are being applied to permit viewing of phenomena that occur faster than the frame rate. Criticisms of IR in the past have been that it lacks resolution, surface effects could not be separated from subsurface, and what was seen was not well-understood. Progress on all of these problems is now being made.

Though the examples to be given here will be from photoacoustic imaging rather than spectroscopy, photoacoustic spectroscopy was the first major area in the revival of photoacoustics and still represents the largest subarea of this field. In spectroscopy, the wavelength of the light making up the excitation beam is varied. Coupling photoacoustic detection to this approach provides a spectroscopy that responds to radiationless transitions expressed as in lattice vibrations or kinetic energy of gas atoms.

The underlying theory of the photoacoustic effect hinges on the concept of the "thermal wave" which the periodic (or pulsed) heating launches into the material. This is a critically damped temperature wave with "wavelength" proportional to the inverse square root of the laser modulation frequency. What follows sketches the development of the basic idea.

The heat equation, developed by considering only the specific heat of a tiny volume in a medium as a source or sink of heat and conduction through its surface for the flow of heat, is

$$\nabla \cdot \kappa \nabla T = \rho c \frac{\partial T}{\partial t}$$

where T is the temperature, κ is the thermal conductivity, ρ is the density, c is the specific heat at constant pressure and t is time. The quantity ρc can be regarded as a volume specific heat. The quantity $\kappa/\rho c$ occurs often enough to have its own name, thermal diffusivity. A one dimensional solution to this differential equation, as can be verified by direct substitution, is

$$T = T_0 e^{-(1+i)\sqrt{\frac{\rho c \pi f}{\kappa}} x} e^{+i 2\pi f t}$$

where T_0 is a constant and f is the modulation frequency. This solution oscillates in time and in space and is critically damped. The real part is regarded as having physical significance. Such a solution is not new. Angstrom published an oscillating solution in 1861; however, the idea seems to be periodically lost in the scientific community. The amplitude of the thermal wave falls to e^{-1} in a distance of $\sqrt{\kappa/\rho c \pi f}$, which is called a thermal diffusion length, and falls to $e^{-2\pi} = 1/535$ in a distance $2\pi\sqrt{\kappa/\rho c \pi f}$, which is called a thermal wavelength. Despite such heavy damping, thermal waves reflect, scatter and interfere in the same manner as more conventional waves. We have given a detailed background for this heat equation and for a one-dimensional solution for the case of a coating on a substrate elsewhere².

The temperature variation occurs primarily in the heated spot. This allows localization of the effects primarily to the heated spot. Thus, resolution is on the order of the focal spot size, and one micron resolution has been demonstrated with laser excitation, and less is possible with modified electron microscopes. For subsurface features, one can see things that are about as big as they are thermally deep.

Considerable literature now exists in this area³⁻⁹.

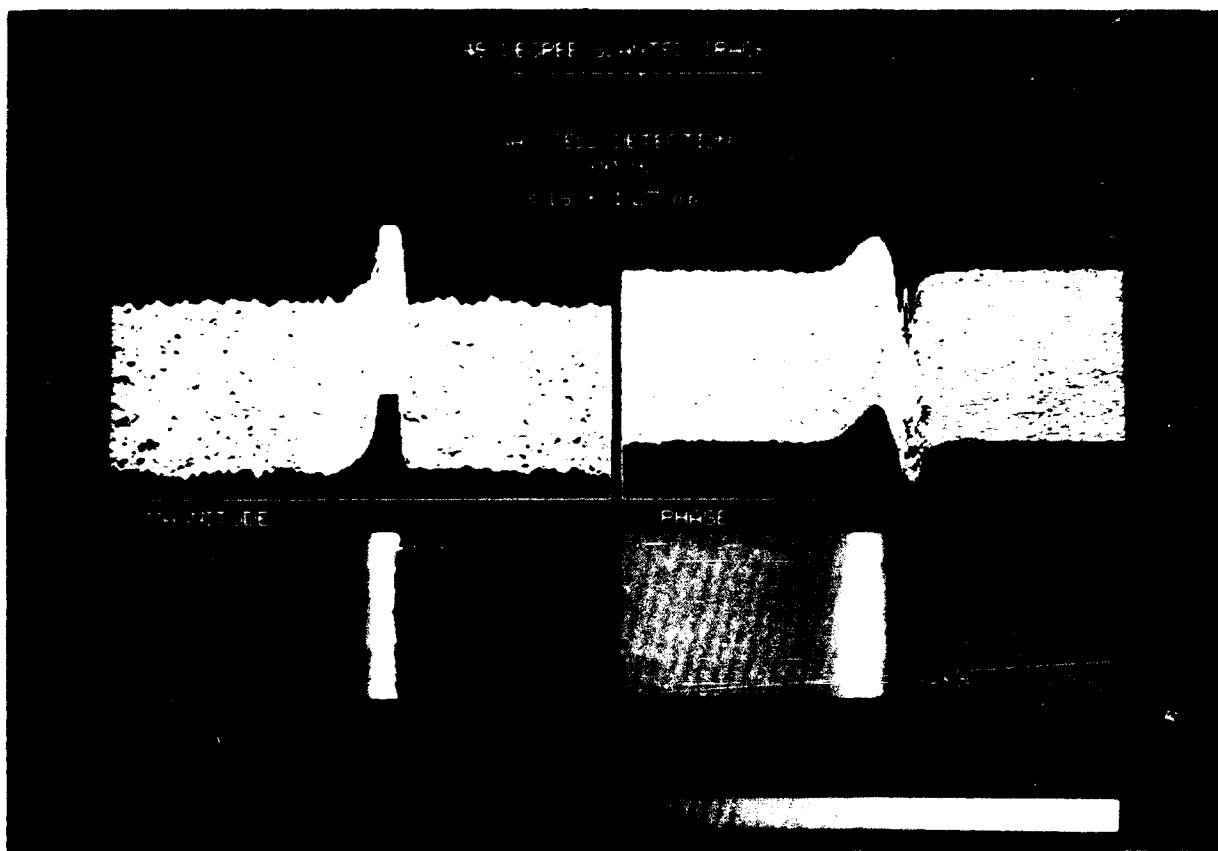
Figure 2. Vertical milling roughness standard.



This set of images is of a 1.6 X 1.6 mm area of one block in a roughness standard which had a series of blocks representative of different machining operations to various finishes. Note that there is a phase to the signal as well as a magnitude. The particular area imaged here, with gas cell detection at a laser modulation frequency of 500 Hz, had a nominal roughness of 3.2 μm Ra or 125 microinches AA. As these images show, surface profile does affect the thermal wave image. The subsurface is presumably uniform, so the image detail arises from the surface profile. Because heat does not have as much material into which to flow from the ridges as from the bottoms of the valleys, the ridges stand out as hotter. If the images were not enhanced, the phase image would show little contrast.

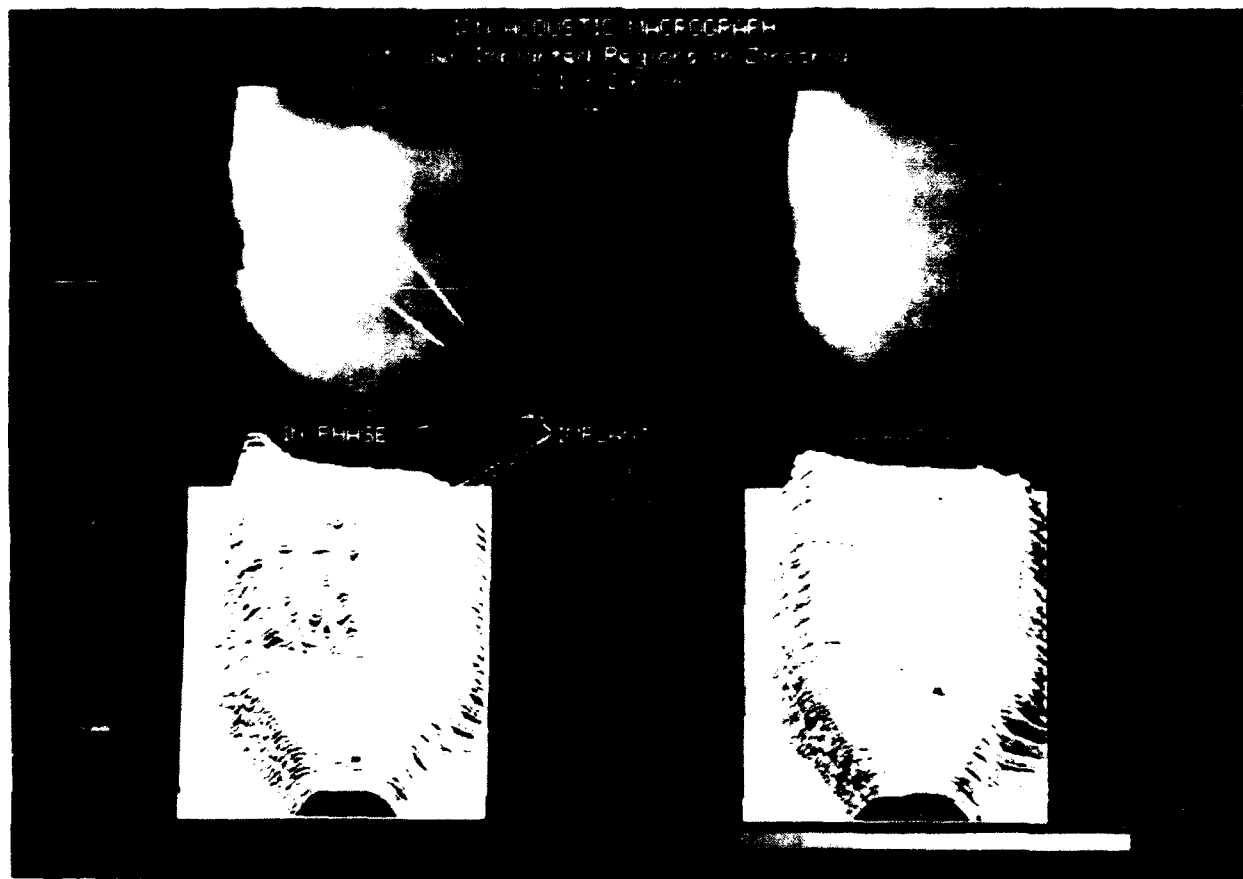
All of the thermal wave images to be shown here were obtained via point-by-point scanning, with the response stored as an array of numbers. At the bottom of this picture, and of a few of the others to be shown, there is a horizontal bar, which in this case shows that lower temperature amplitudes are white and higher ones dark, an inverse display. Unless otherwise shown by the bar, the displays here have the higher values white.

Figure 3. 45 slanted crack.



This sample was constructed at Wayne State University, Detroit, Mich., by milling two aluminum blocks at 45°, gluing them together and then polishing the surface so that the joint was not visible. In the images, the slanted "crack" descends towards the left, as depicted by the lines under the title. Gas cell detection was used. An area of 3.18 X 1.27 mm is shown. The upper two images are graphical presentations of the data; the lower two, video displays. The left two are of the magnitude of the thermal wave; the right two are representations of the phase. The response to the subsurface "crack" dominates the images. The response in the magnitude is truncated and, thus, the considerably smaller response from the surface scratches on the aluminum can be seen, provided the reproduction of the photograph is good. As the phase primarily responds to subsurface features, the polishing scratches are not seen in it. As can be seen by the width of the response to the slanted crack, the phase "sees" about twice as deeply as the magnitude.

Figure 4. Ion acoustic macrograph.

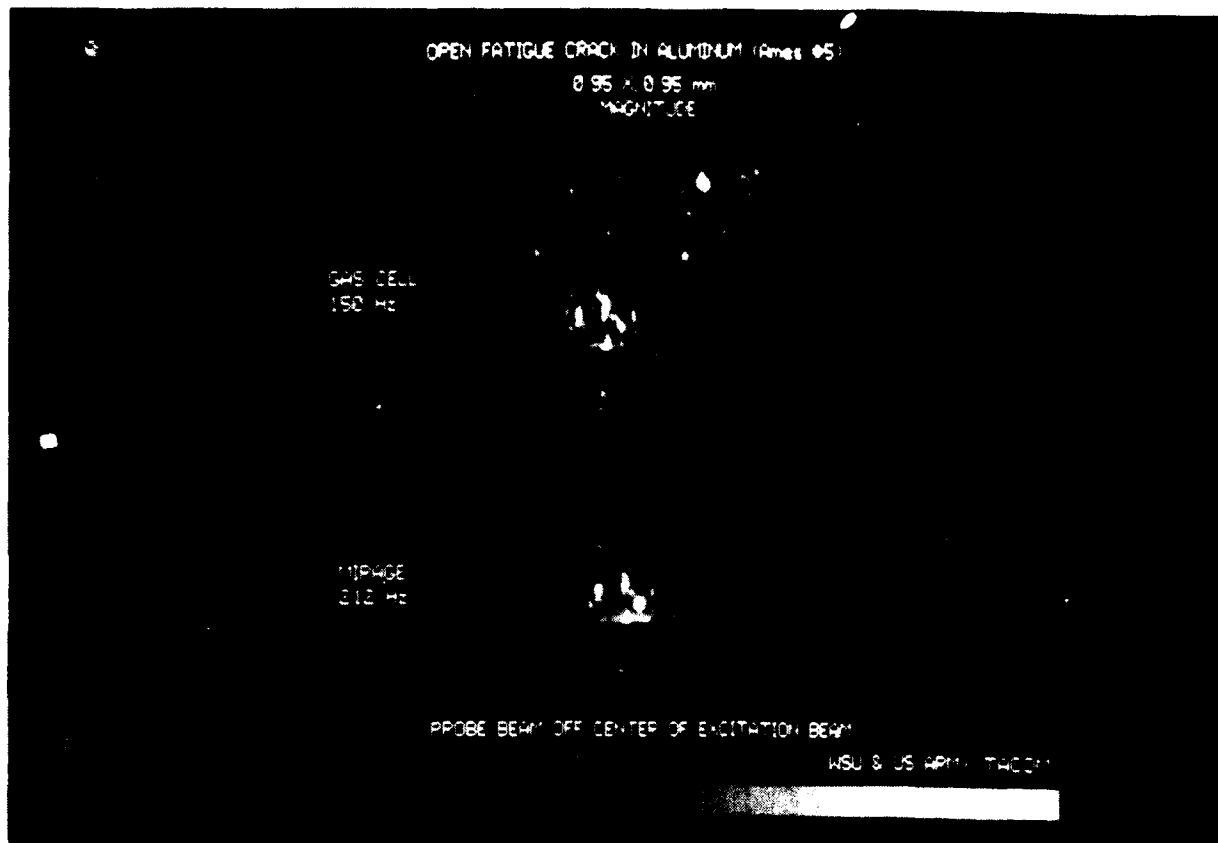


These images illustrate that the excitation beam does not have to be a laser. These images are of a slab of cubic zirconia which had two spots previously implanted with nitrogen. The slab was later imaged with a modulated ion beam. Except for the top of the slab which was truncated in these images, the shape of the slab can be seen. Though there are only 32 X 48 points in these images, the implanted areas are clearly visible. The top two images are video displays; the bottom two, graphical displays. The left two images are in-phase data; i.e., the response that is in-phase with the modulation of the ion beam, and the right two images are of the response 90° out of phase with the beam modulation. Consistent with the implantation being quite near the surface compared to the thermal wavelength, the implantations are only visible in the in-phase image.

These images were made by detecting the sample vibrations inside an implanter used for implantation studies rather than in a specialized research analysis tool. They graphically illustrate the possibility for using photoacoustics to control ion beam implantation *in situ* or to control laser modification of surfaces *in-process*.

The ion implantation pattern in semiconducting wafers is now being displayed commercially using a system which utilizes laser beam excitation and photoreflective detection.

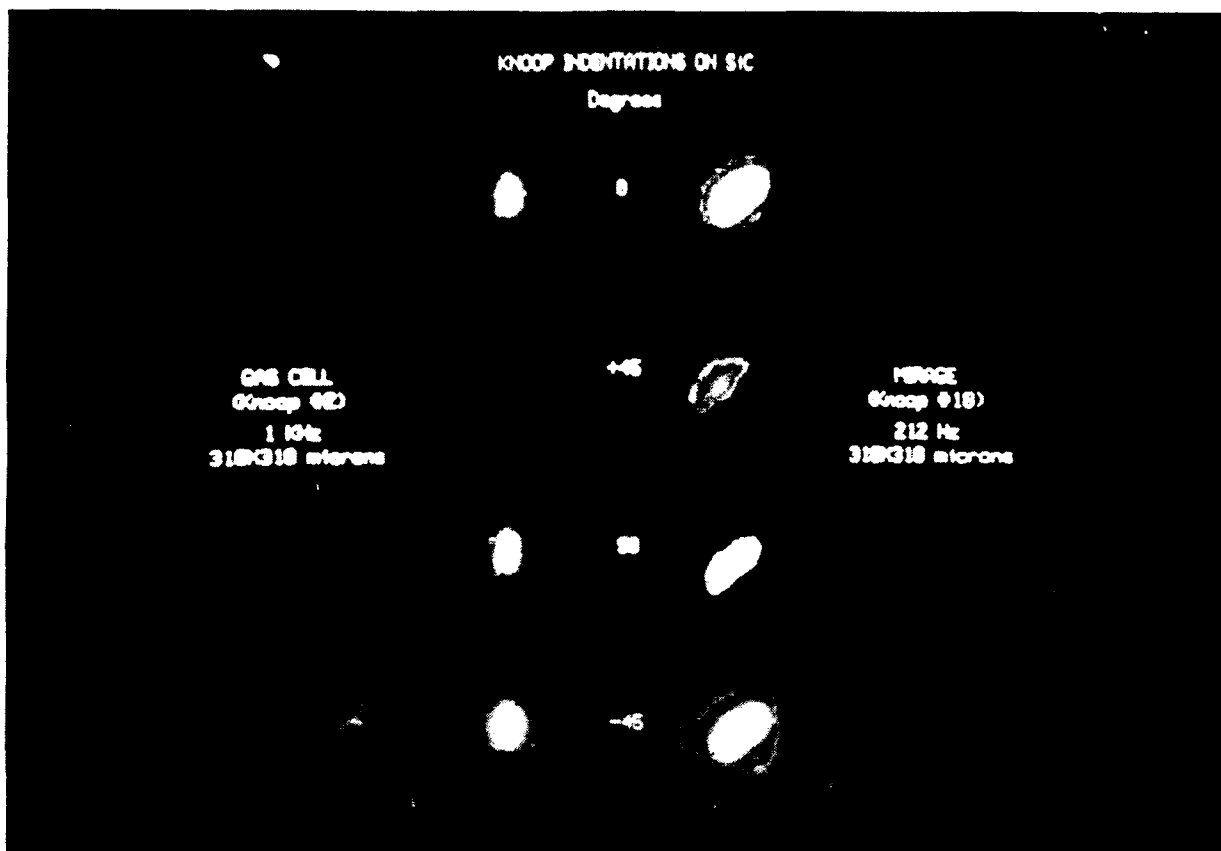
Figure 5. Fatigue crack in aluminum imaged with both gas-cell and mirage detection.



This sample of aluminum had a fatigue crack which was held open by an external frame. The response to the crack, using both gas-cell and mirage detection, is depicted. That the response is different is to be expected. For the lower mirage image of the 0.95 X 0.95 mm area, the probe beam was off the center of the focal spot of the heating laser. The distinctive black/white signature of vertical cracks, using mirage detection with the probe laser beam offset in this manner and at least partially aligned with the crack, is clearly displayed.

Gas-cell detection does not see perfectly vertical closed cracks. In practice, gas-cell detection does see most cracks, because they are usually neither perfectly closed nor perfectly vertical.

Figure 6. Comparison of gas-cell and mirage detection of Knoop indentations on sintered SiC.

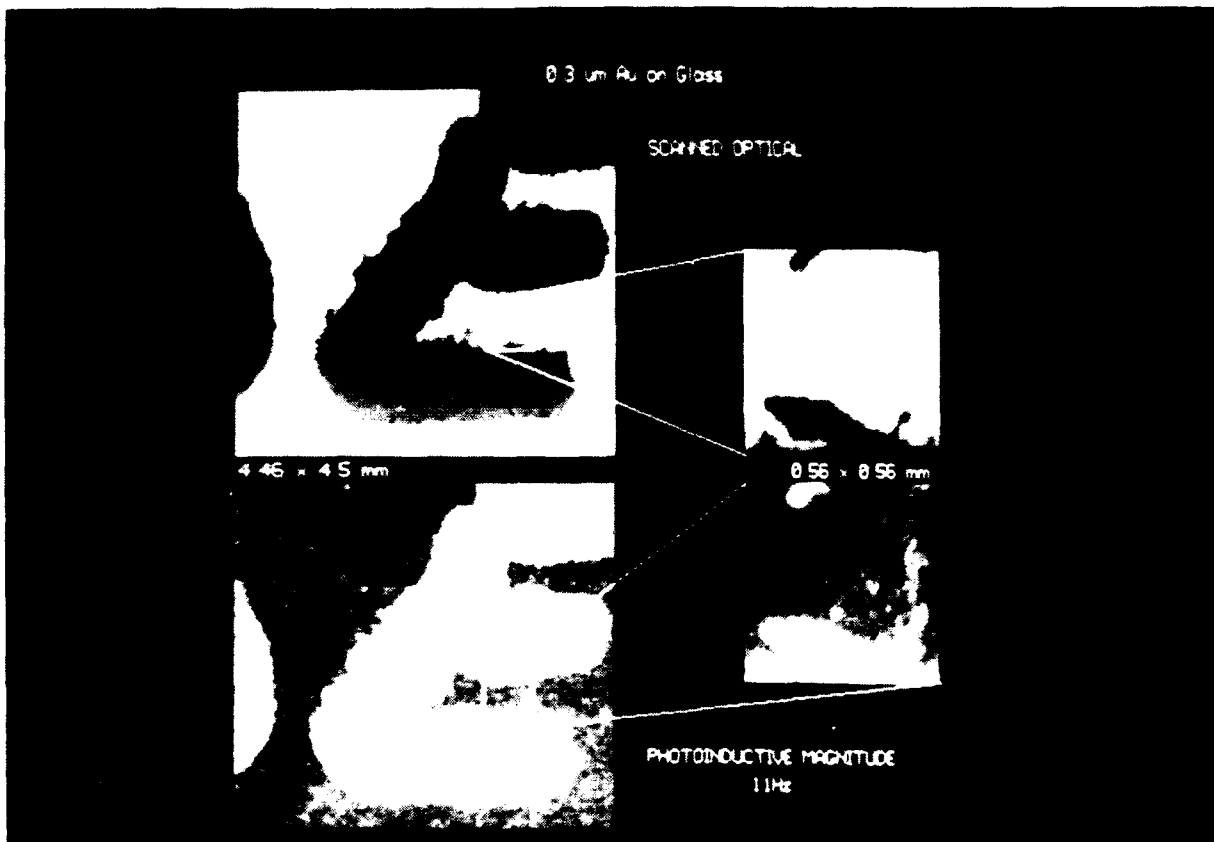


The images are of a 318 X 318 μm area of two different Knoop indentations on sintered silicon carbide (SiC). The images on the left result from gas-cell detection of one of the indentations; the ones on the right result from mirage detection used on the other indentation. A comparison of the results at four different fixed phase angles is shown.

Knoop indentations are made with elongated pyramidal diamond points and are often used for measuring the hardness of materials. They induce lateral cracks and a vertical crack along the long axis of the indenter. The surface indication is about 1/2 of the height of these images but only 6 % of the width. The surface indication corresponds to what is visible in the gas-cell detection image at +45°.

While the mirage and gas cell indications are different, they both show maximum response at -45° and minimum response at +45°, as expected from one dimensional theory for shallow cracks. These images again demonstrate subsurface imaging capability using thermal waves.

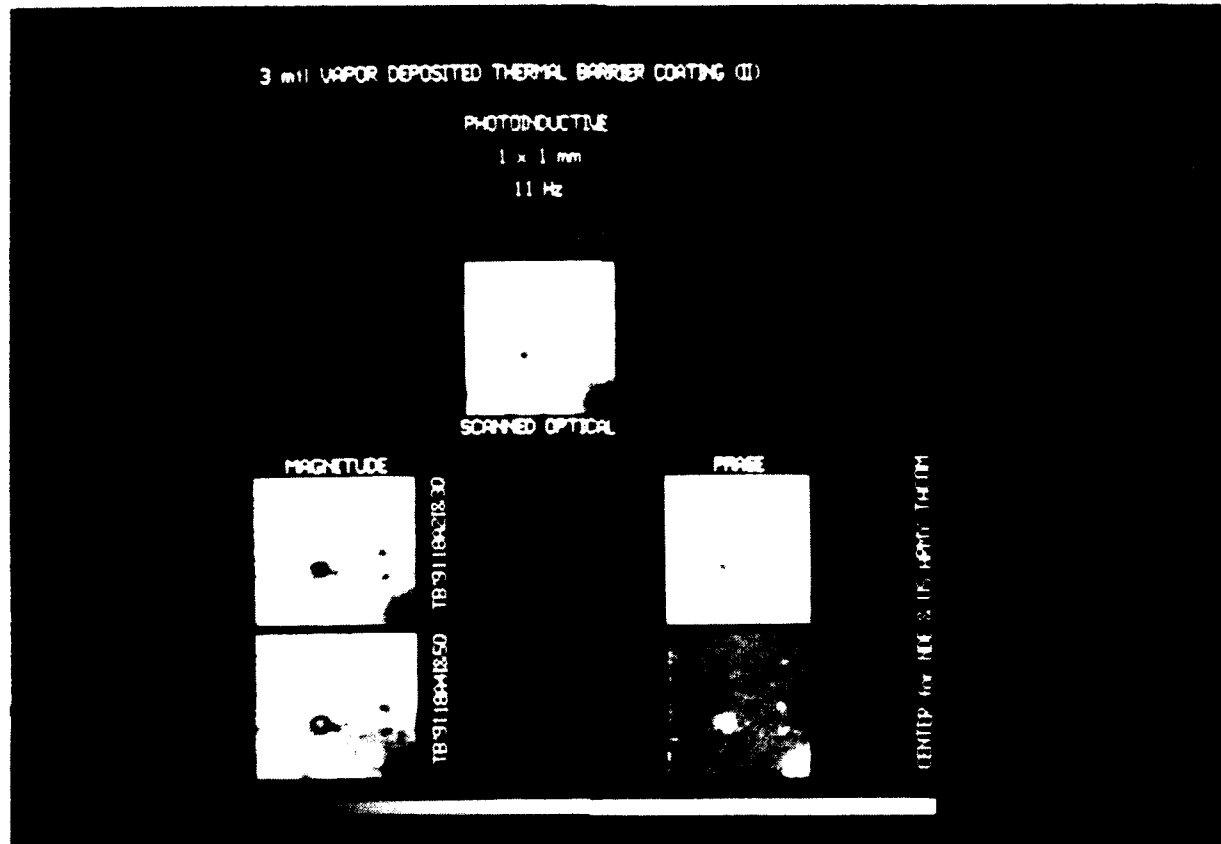
Figure 7. Resolution demonstration with eddy-current detection.



These images illustrate the increased resolution attainable by combining eddy current technology with photoacoustic microscopy concepts. This has been called photoinductive imaging. Two scans of an "E" in "NDE" which was written in ink on a $0.3\text{ }\mu\text{m}$ thick gold/chrome film on glass are shown. The upper images are scanned optical images obtained concurrently with the photoinductive magnitudes displayed in the lower two images. The images on the left hand side are of an area $4.46 \times 4.5\text{ mm}$ and include some of the curve from the "D" in "NDE" as well as the "E". The images on the right are of a $0.56 \times 0.56\text{ mm}$ area of the "E". Features down to $20\text{ }\mu\text{m}$ were discernable.

The resolution here is equal to 0.5 % of the size of the eddy-current coil and represents orders of magnitude finer resolution than has typically been obtained with eddy-current imaging. The eddy-current frequency was 30 MHz; the thermal wave frequency, 11 Hz. Resolution down to $1\text{ }\mu\text{m}$ should be attainable with this approach.

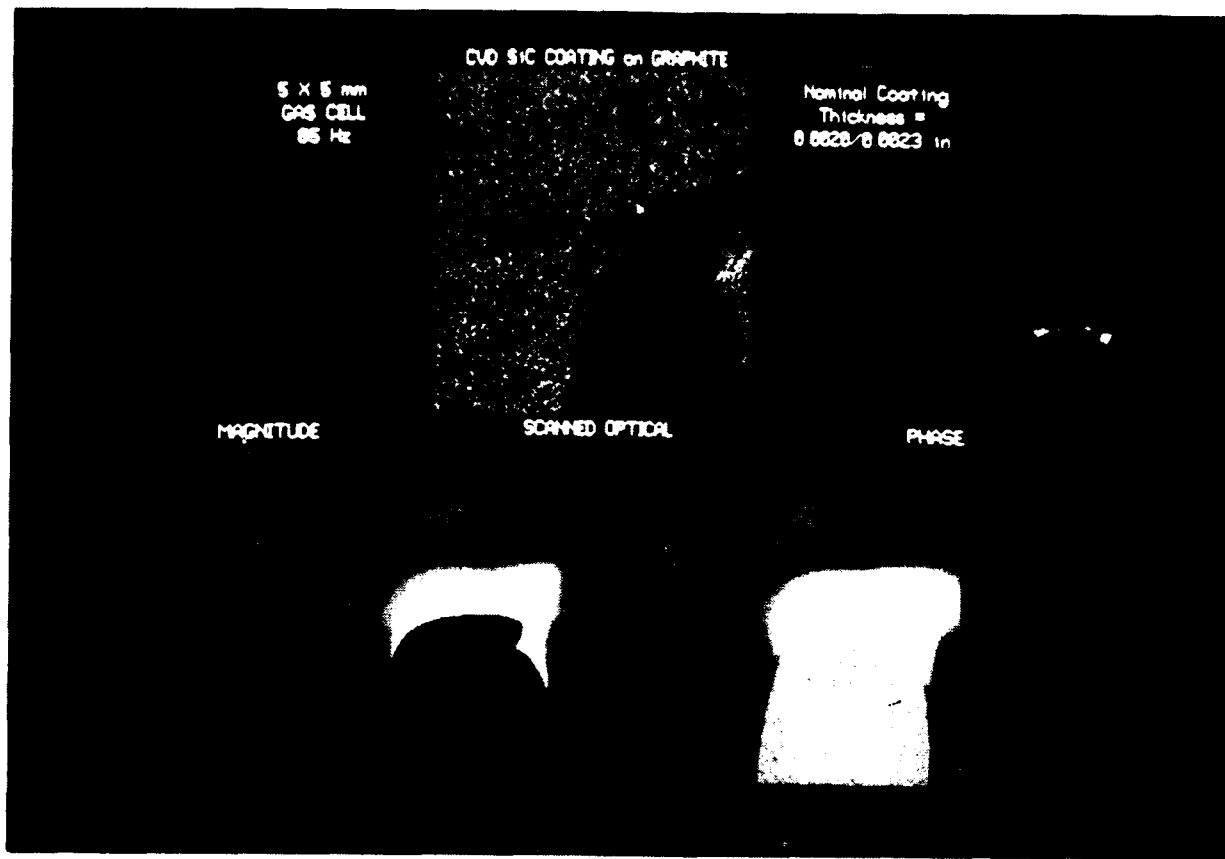
Figure 8. Photoinductive images of a thermal barrier coating.



The 1 X 1 mm area imaged here is of a 75 μm thick yttria stabilized zirconia thermal barrier coating deposited onto a nickel-based superalloy. A scanned optical and two concurrent sets of magnitude and phase images from different lock-in amplifiers are shown. A pore in the coating is clearly resolved, though the thermal wave had to penetrate through the coating and into the metal substrate to be detected. Since the signal detected depends directly on the thermal impedance of the coating, this is a promising method to inspect coatings.

What is shown in these images can still be attributed to optical contrast mechanisms acting in the eddy-current detection system. Currently, efforts are in progress to separate the contrast due to photoinductive sources and that due to optical causes.

Figure 9. Chemical vapor deposited SiC on graphite.

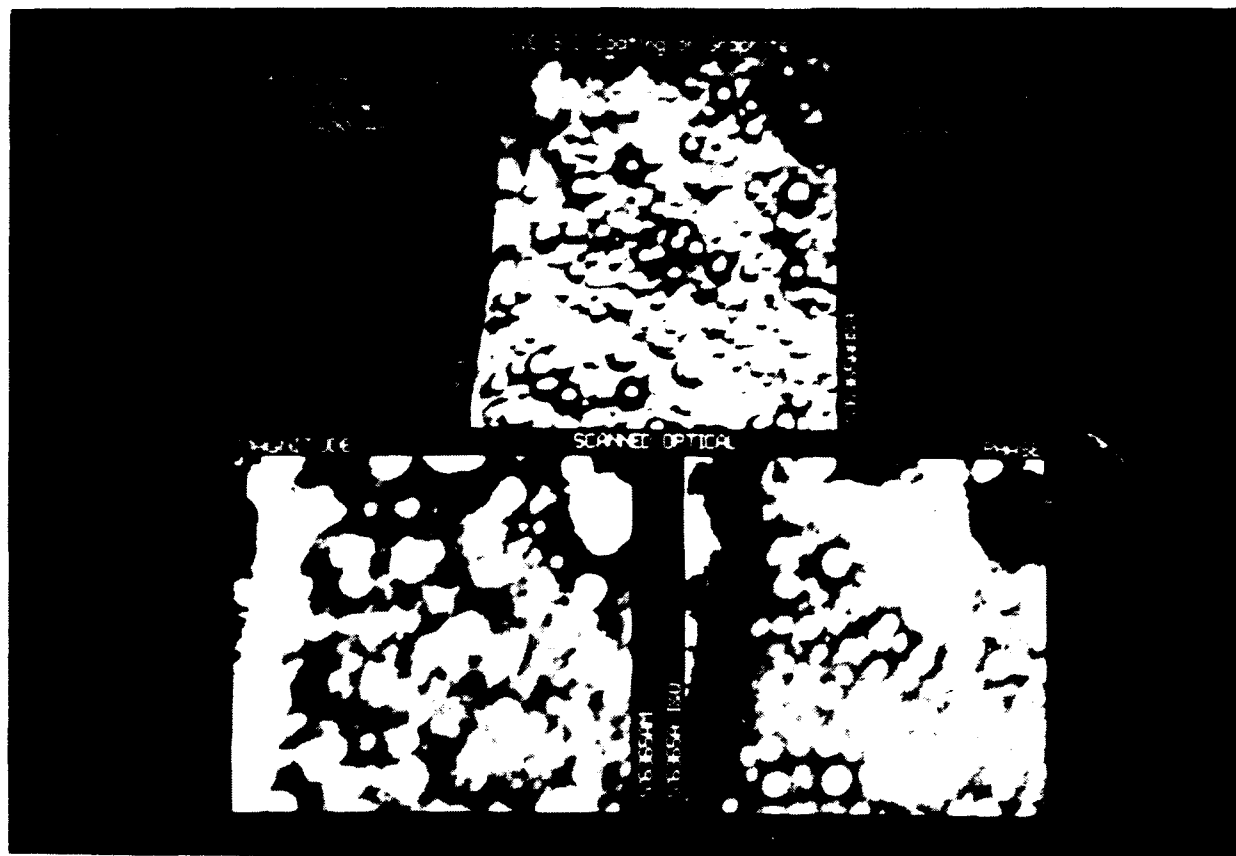


SiC was deposited using chemical vapor deposition (CVD) on substrates of graphite, sintered alpha SiC, zirconia and mullite in three different nominal thicknesses[†]. Before the coatings were deposited, graphite paint was painted onto the substrates in a tic-tac-toe pattern to give a known subsurface structure.

The figure shows a 5 X 5 mm area of one of the coatings. The graphite paint can be seen under the coating in the photoacoustic images as broad stripes at the top of the images and on the right hand side also. The coating spalled off in a region visible in the lower right of the images. Apparently, the coating is separated from the substrate over the graphite paint at the top of the spalled area, as shown by the bright area just above the spall in the photoacoustic images. The coating thickness was measured as 55 μm , the nominal value, at the top of the spalled region and 25 μm at the thinnest point on the right side of the spalled region at the bottom of the image.

[†]San Fernando Labs, Pacoima, CA

Figure 10. Images of the right-hand edge of the spalled region.

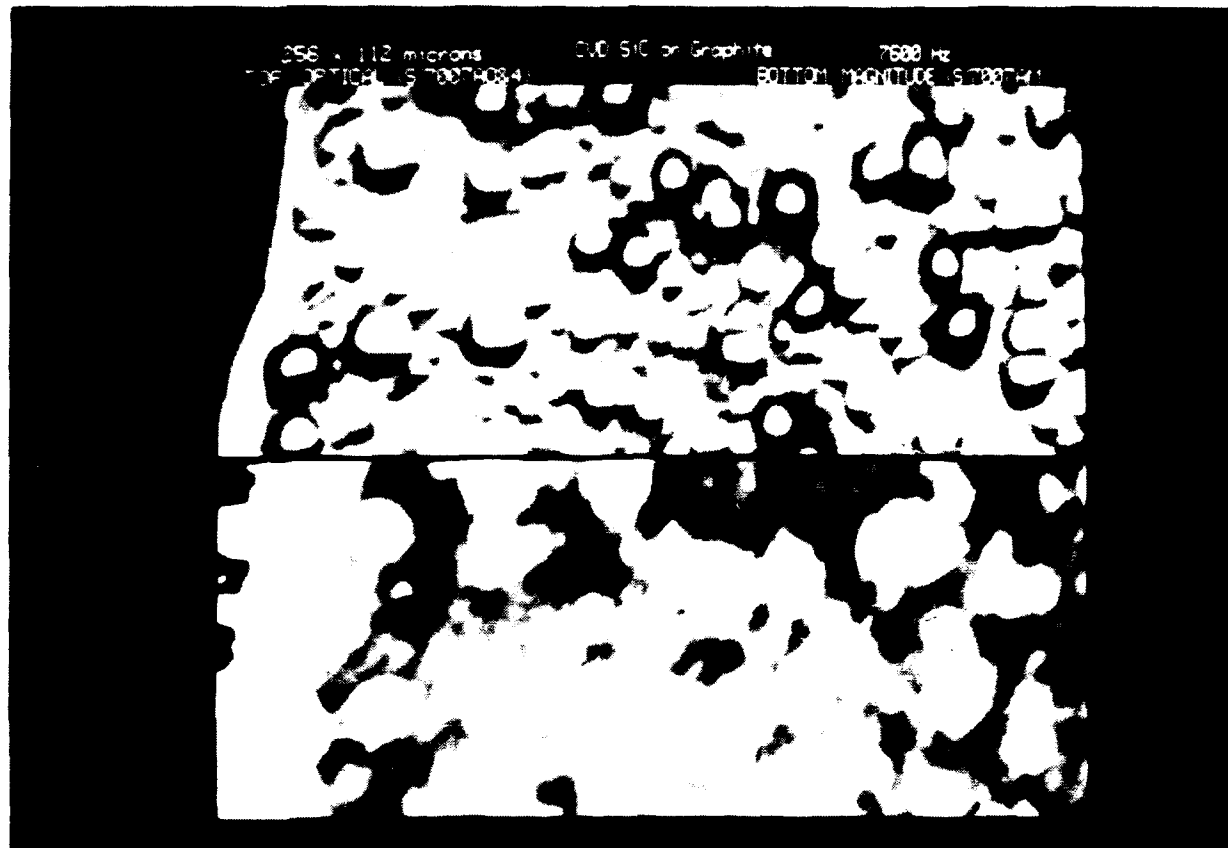


This set of images of the right-hand edge of the spalled region in the previous figure and the next set of images will be used to show the resolution available with this technique. They have been enhanced with an image processing technique, called "equalization", to bring out the middle tones. Otherwise, the strong photoacoustic response at the edges would overpower the finer image detail. The edge of the spall is on the left-hand side in these two sets of images.

The enhanced magnitude looks rather like cotton balls loosely strung together. The enhanced photoacoustic phase looks rather like cotton balls dropped into a box. This is characteristic of these high-resolution images.

For features to use for substantiating resolution, we chose line pair like structures, since they are the simplest discernable patterns not attributable to noise. Lines parallel to the scanning direction are suspect and were excluded from consideration.

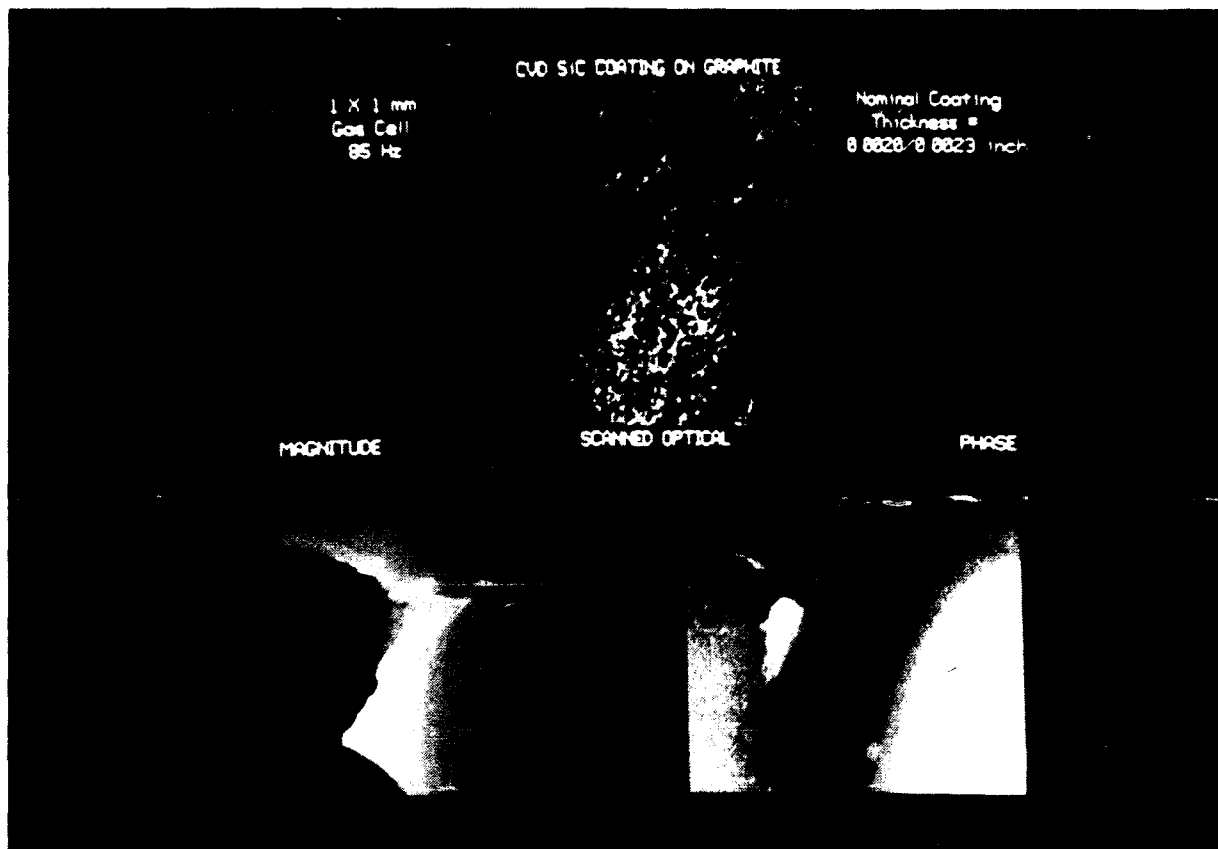
Figure 11. Images with 1 μm features.



These two equalized images are of the lower half of the area of the previous figure at a step size of 0.5 μm . Limitations of our display system precluded simultaneous display of the photoacoustic phase. In the original images several areas with 1 μm features could be seen. In the accompanying photoacoustic phase image, features down to 2 μm were found.

1 μm resolution is consistent with the Rayleigh criterion limit for the 3.4 μm focal spot size of the laser beam used for these images.

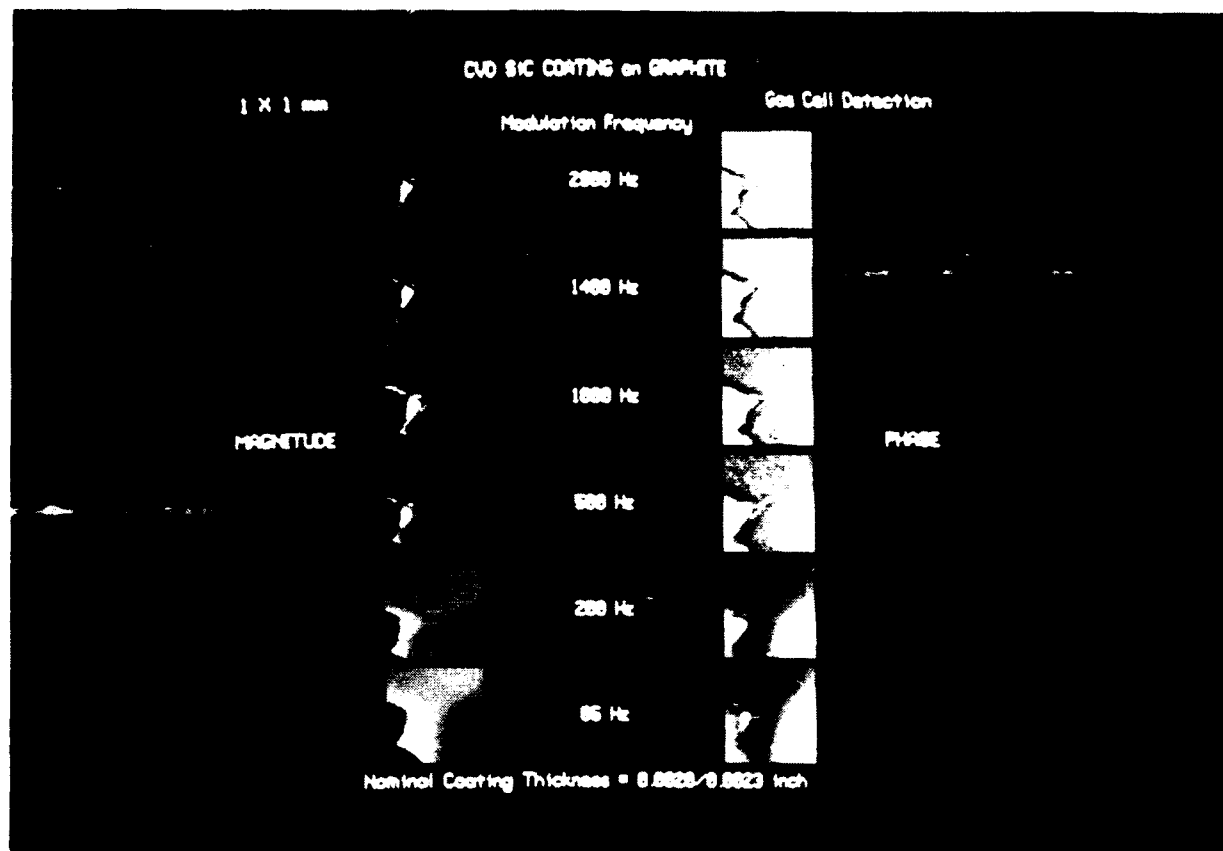
Figure 12. A 1 X 1 mm area of Figure 9.



This shows enlarged images of the sharp corner projecting into the spalled area in Figure 9. As the spalled chip broke off, it left steps in the region between the point and the rest of the coating which can be seen in the thermal wave images but not in the scanned optical, because the scanned optical only sees spectrally reflected light, and the steps are somewhat angled. There is an area about $60 \times 23 \mu\text{m}$ in size just above the area of the steps on the edge of the unbroken coating. Under a microscope, this appeared to be a tiny chip which had not quite broken off. The upper 1/4 of the image is over the apparent delamination under the coating. In the lower right of the images, the coating is directly on the graphite substrate. In the lower left is the spalled area.

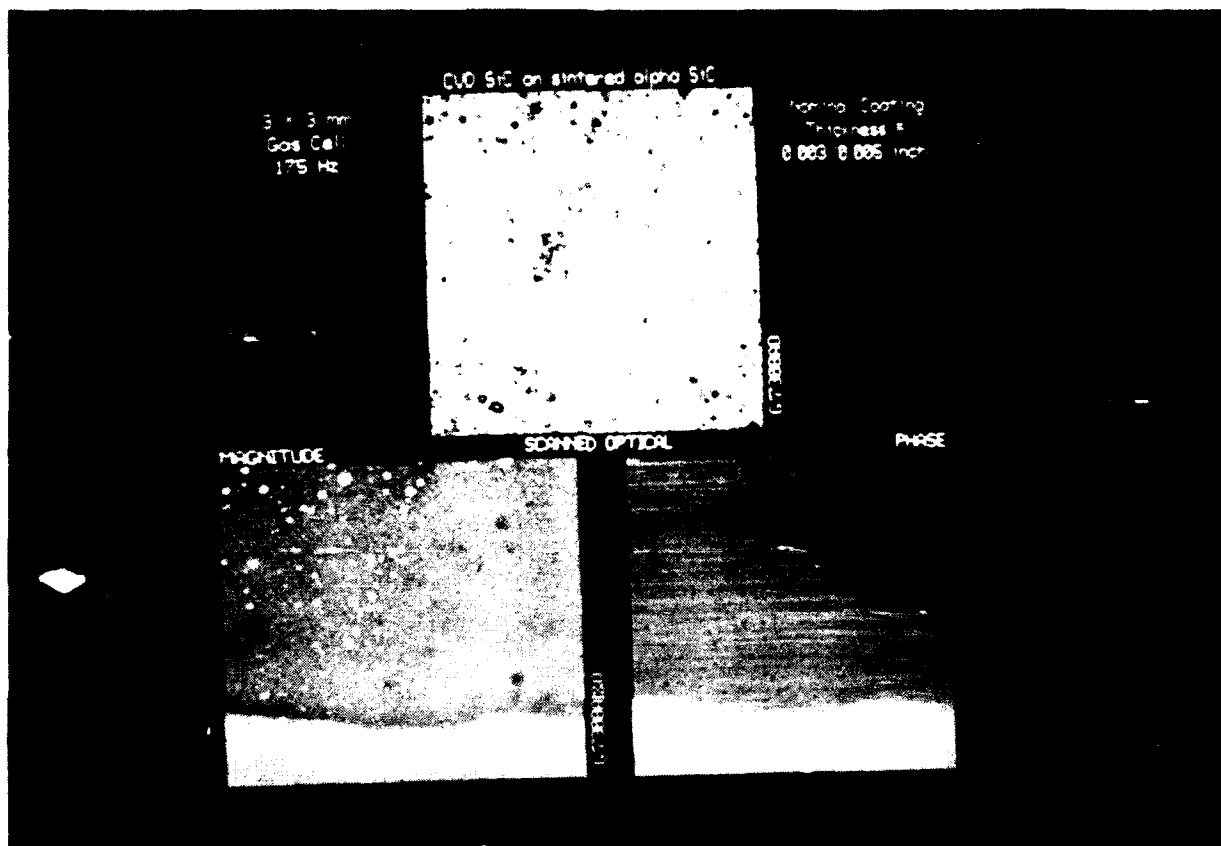
Though the thermal wavelength, based on bulk properties of CVD SiC, is 2.5 mm, which is longer than the entire image, the resolution of features near the surface is quite sharp. This is typical of thermal wave images.

Figure 13. The area of Figure 12 at different modulation frequencies.



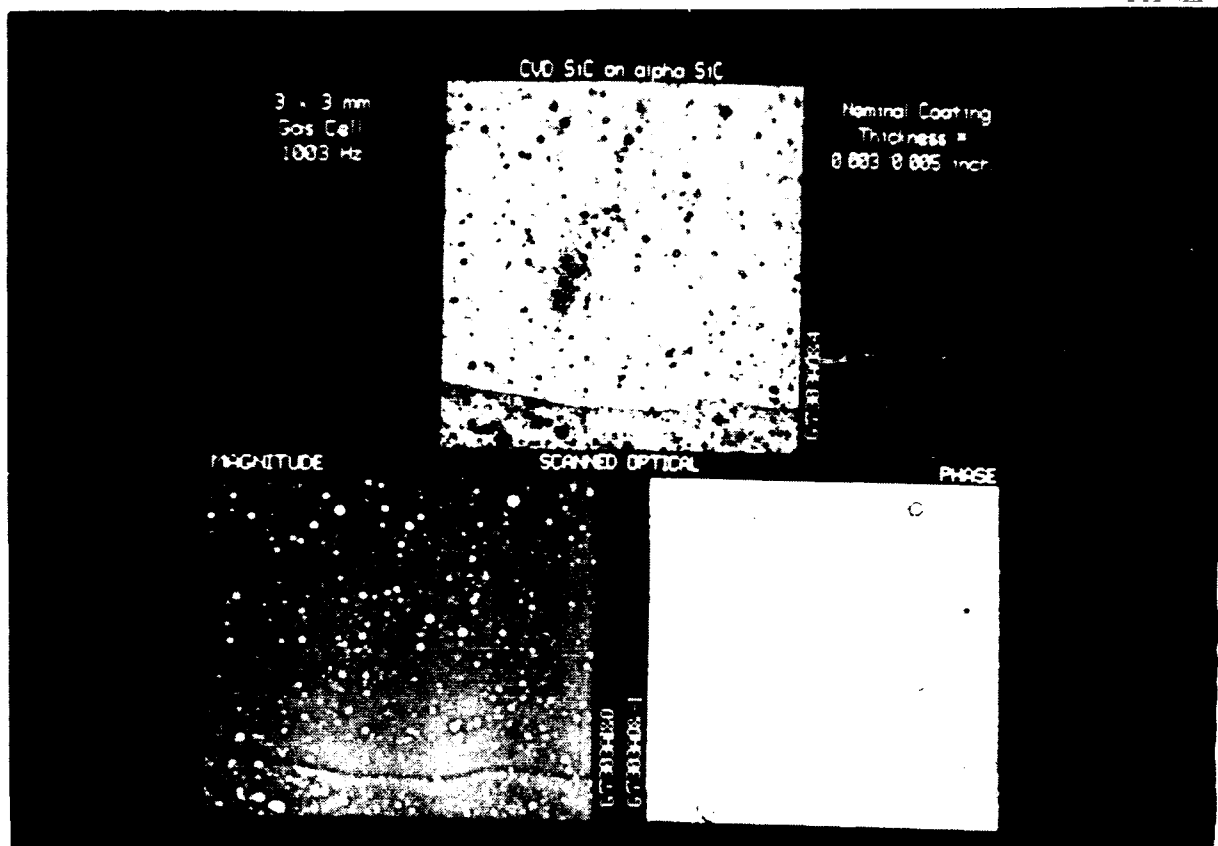
This set of thermal wave images shows the magnitude and phase response of the area of Figure 12 at laser modulation frequencies from 2.9 KHz to 85 Hz. Particular attention will be paid to the lower right-hand quarter of the images where the coating is in direct contact with graphite in contrast to the upper right-hand quarter where the coating is on the graphite paint. Beginning at 1.4 KHz, the difference in substrates is seen in the phase images, while this distinction only becomes barely apparent in the magnitude images at 500 Hz. At 2.9 KHz, the thermal wavelength does not allow us to see through the coating. However, in the corner where the broken steps were formed, thermal wave interference effects are already visible at 2.9 KHz. The changes in this small corner area of thinner coating thicknesses can be compared as the modulation frequency is lowered. Even in these 64 X 64 point images, the 23 X 60 μm area that is above the corner region which was referred to in Figure 12 can be seen as a tiny white area, especially in the magnitude images.

Figure 14. CVD SiC on sintered α SiC.



This sample is similar to the previous sample in construction, except that the nominal coating thickness is 100 μm thick and the substrate is sintered alpha (α) SiC. This image of a 3 X 3 mm area is at 175 Hz. In this image, the graphite paint is under the coating in the bottom 20 % of the image. The difference in substrate for the coating, directly on sintered alpha silicon carbide in the upper 80 % and on top of graphite paint which is in turn on top of the sintered silicon carbide in the lower 20 %, can be seen in the thermal wave images. The difference in substrates could also be seen at 500 Hz.

Figure 15. CVD SiC on sintered α SiC. The area of Figure 14 at 1 KHz.

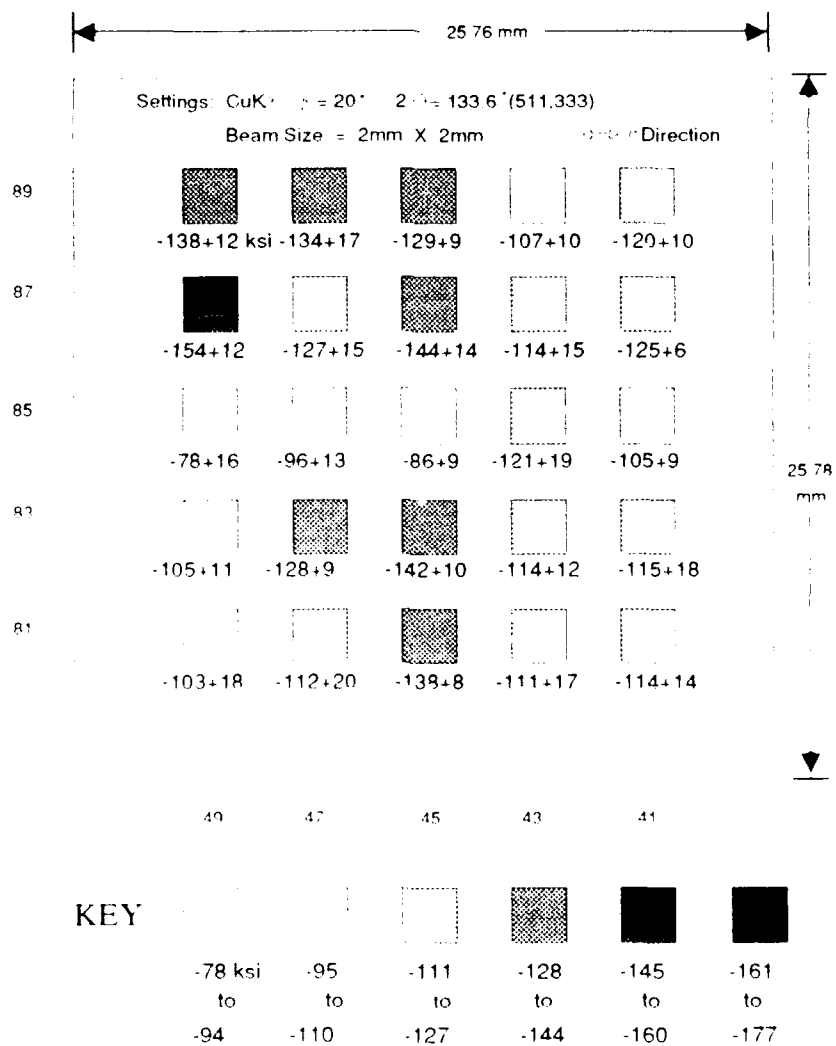


These images taken at 1003 Hz are of the same area as in Figure 14. The photoacoustic magnitude and phase are not influenced by the differences in substrate for the coating in the upper 80% and lower 20% of the image, as they were in Figure 14.

Using the preliminary data from a comparison of these image sets in Figures 13, 14 and 15, and other scans in which the modulation frequency was varied on these and other samples with this construction, a thermal diffusivity of $0.04 \text{ cm}^2/\text{sec}$ is suggested, rather than the $0.6 \text{ cm}^2/\text{sec}$ value obtained from tables of the bulk properties of CVD SiC. However, this result requires further confirmation.

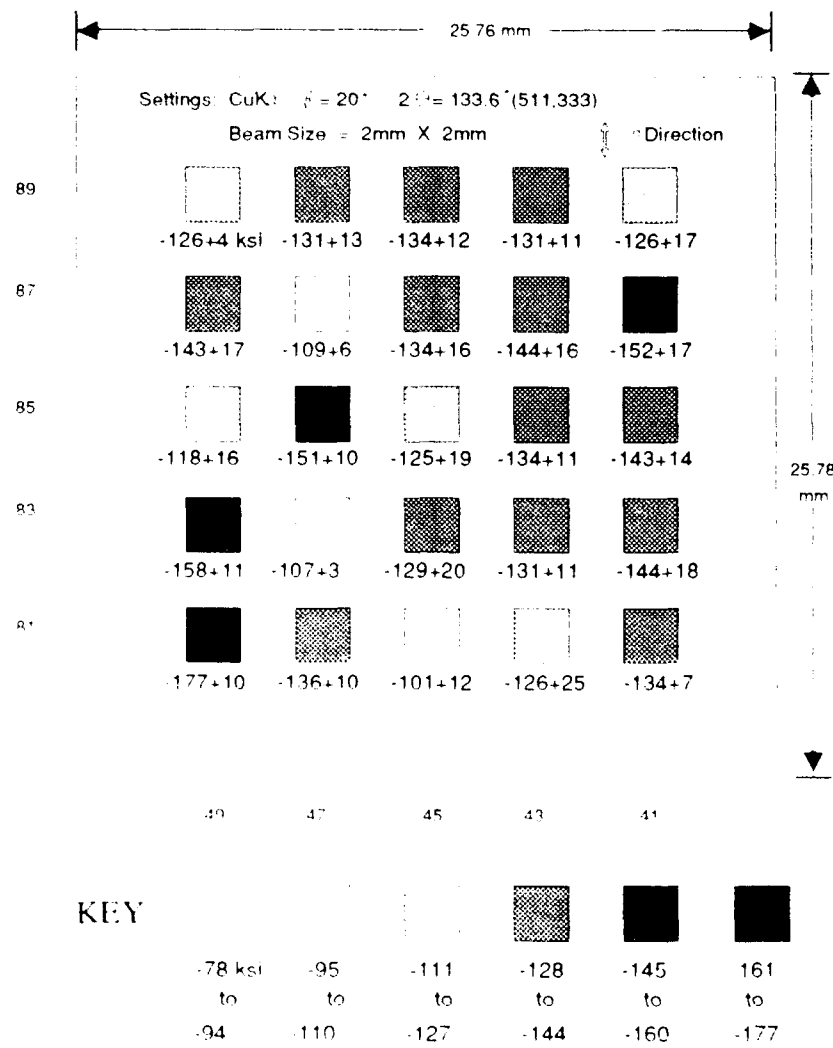
These results have application in considering the behavior of coatings in engines in situations where the thermal energy incident on the coatings is rapidly changing. It appears that surface roughness can act as a porous coating with reduced thermal diffusivity. Work is in progress on theory and experiment to support this.

Figure 16. Residual stress in CVD SiC sample 3B || to 49-41 edge.



The residual stress in two samples, 25 X 25 X 8 mm, of CVD SiC on graphite was measured in two orthogonal directions in a 5 X 5 array of 2 X 2 mm spots at Penn State^{10,11}. The coatings had nominal thicknesses of 200 to 250 μm . There was again a tic-tac-toe pattern of graphite paint on top of the graphite substrate with strips that were approximately 2 X 155 mm on top of which the coating was deposited. The results in ksi on one of the samples, 3B, is shown in these two figures. The numbers along two edges in the figure refer to reference scales which were mounted beside the specimen to allow repositioning for future measurements.

Figure 17. Residual stress in CVD SiC sample 3B \perp to 49-41 edge.

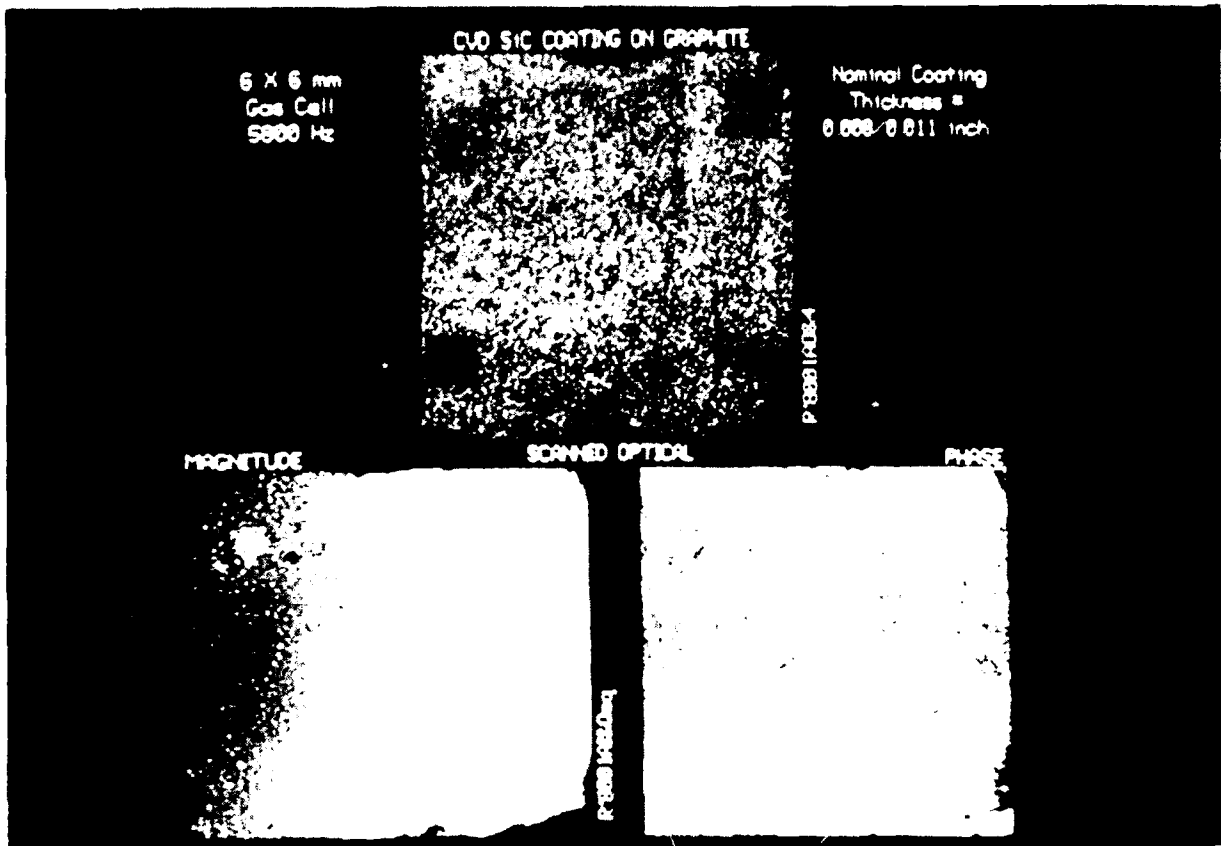


This figure gives the residual stress results in the direction orthogonal to the previous figure on sample 3B, CVD SiC on graphite.

All stresses were highly compressive and of about the same magnitude in the two directions, indicating a uniform stress over the surface with no apparent pattern. There was no discernable effect from the paint under the SiC coating. A preferred orientation of the (111) crystallographic planes parallel to the surface was found.

On sample 3B the stress averaged - 869 MPa (-126 ksi). On sample 3A (not shown) the stresses averaged - 1024 MPa (- 149 ksi). the highly compressive residual stress indicated in these results may be a major factor in allowing these coatings to provide an oxidation barrier for carbon substrates.

Figure 18. Overall scan of locations irradiated with high laser power.

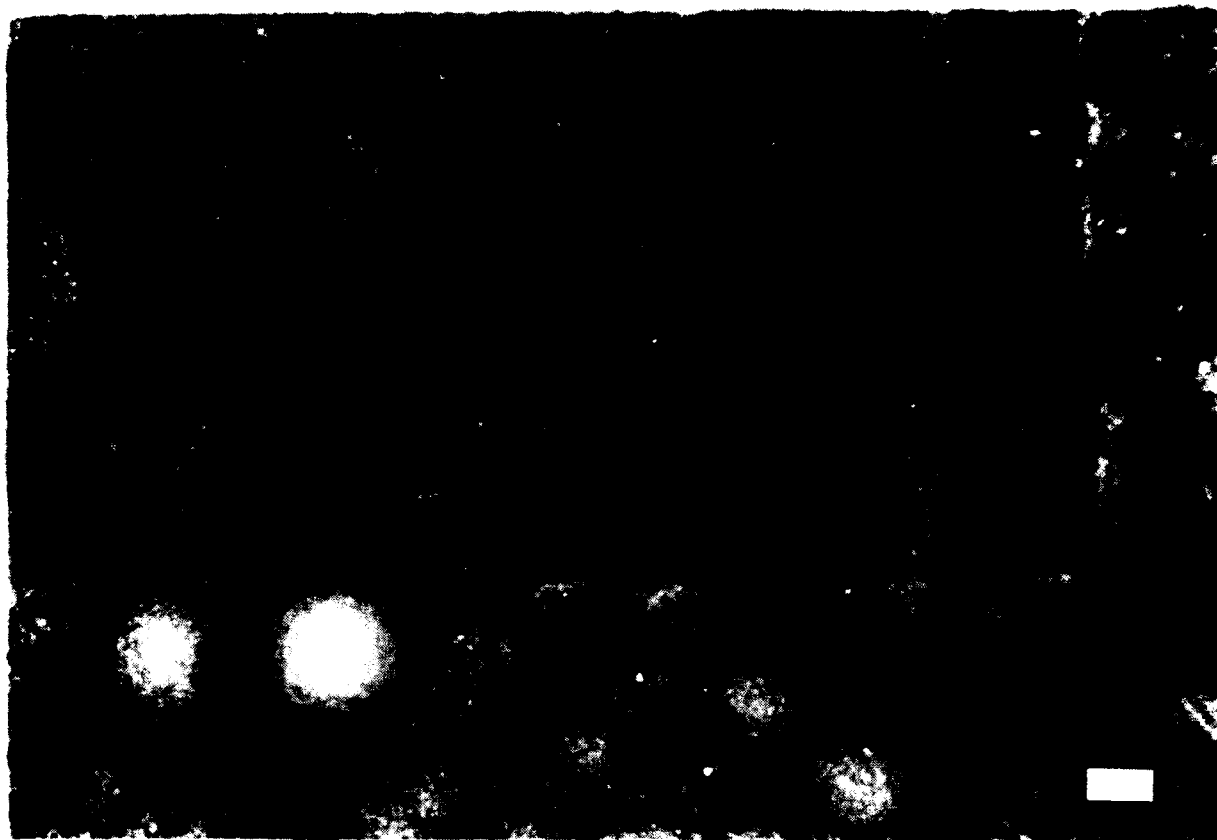


To examine the effect of laser irradiation, four locations on sample 3B were irradiated with high laser power. Photoacoustic scans were done before and after the high power scans, and the photoacoustic signal was also recorded during the high power scans. The above shows a subsequent large area scan. The irradiated locations were labeled 1, 2, 3 and 4, beginning at the upper left in these images and going clockwise. At location 1, the laser was not able to maintain its power. No effects were seen in the scanned optical or photoacoustic signal for that location in the upper left of this large area scan.

The laser power, focal spot size, step size of the scan, dwell time at each step and scanned area size are given below:

Location	Step Size (μm)	Scanned Area (mm)	Dwell Time (msec)	Focal Spot (μm)	Incident Power (mW)	Average Intensity (GW/m^2)
2	4.5	1 X 1	480	6.8	150	0.87
3	4.5	1 X 1	520	6.8	170	1.0
4	3.4	.75 X .75	520	3.2	180	5.2

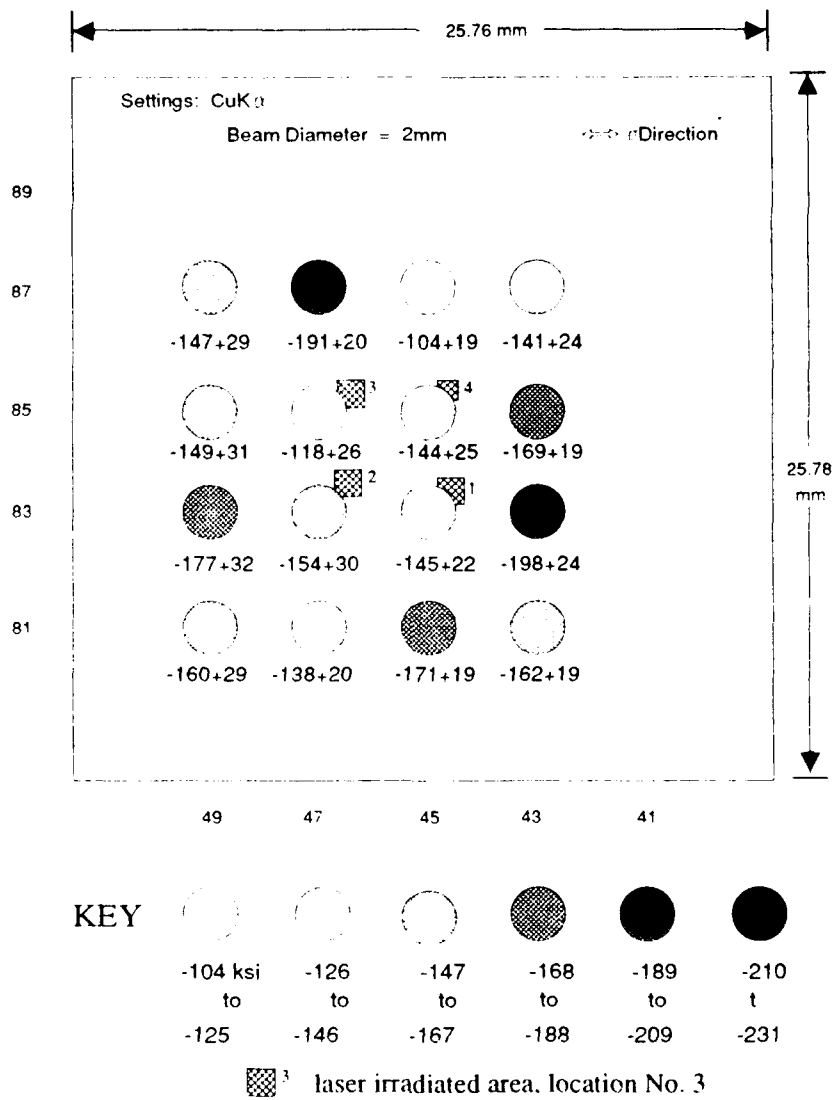
Figure 19. Optical micrograph of corner of area irradiated with highest laser power.



Location 4 had the highest intensity irradiation. The above optical micrograph shows a corner of that irradiated area. The pattern left by the scan tracks can be seen. The marker in the lower right is 20 μm .

For power delivered to the surface up to 40 mW, with an average intensity in the focal spot of 0.27 GW/m², via the 25X objective, and for delivered power up to 30 mW, with an average intensity in the focal spot of 0.8 GW/m² via the 50X objective which had a focal spot of 3.2 μm , the exposure is nondestructive. However, for powers near these levels, scanning tracks have been observed. These tracks show color as if they are formed of a thin oxide coating, but they disappear after storage for a few weeks.

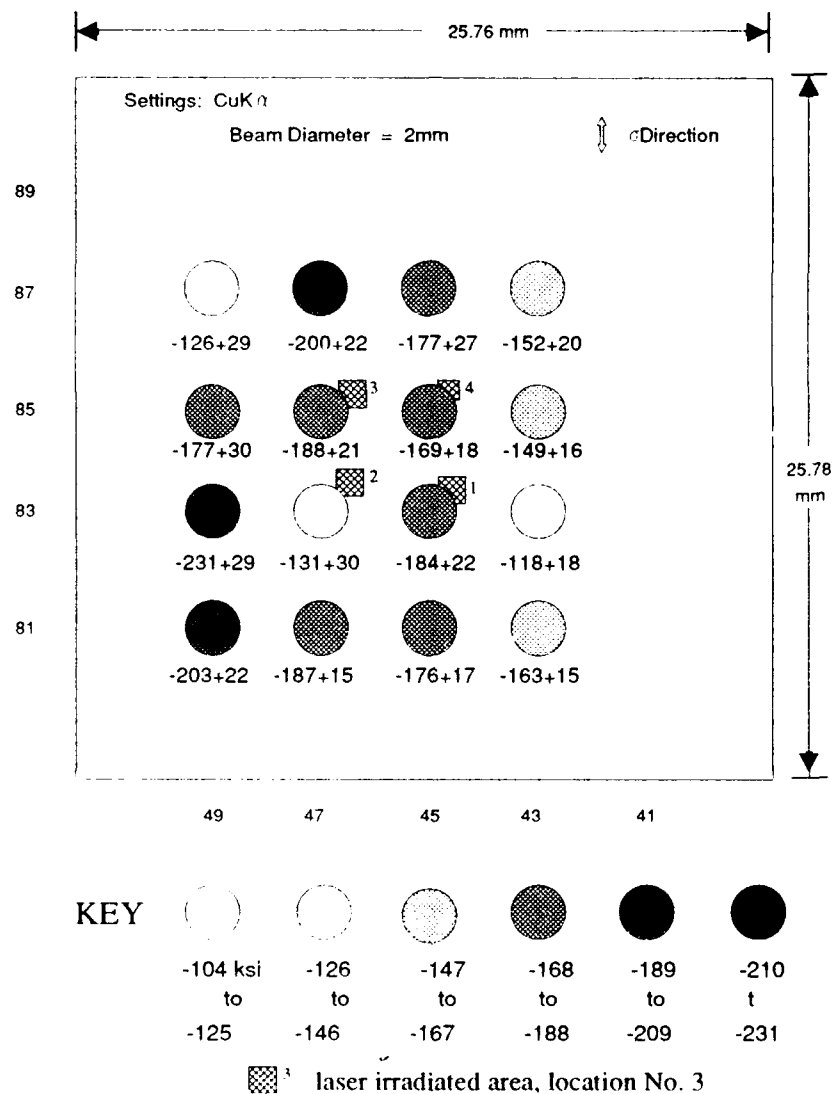
Figure 20. Postlaser irradiation residual stress || to 49-41 edge.



Subsequent to the laser irradiation, the residual stress in the coating of sample 3B was measured at the US Army Materials Technology Laboratory¹² on a different x-ray diffraction machine. These two figures show the results.

There was no effect discernable in these results from the laser irradiation. It can be seen that, unfortunately, the laser irradiated locations are small compared to the size of the areas in which the x-ray beam interacts with the coating. Further, it can be seen that the laser irradiated locations did not fall within the spots measured by x-ray diffraction.

Figure 21. Postlaser irradiation residual stress \perp to 49-41 edge.



To irradiate a larger area at the highest intensity available with our laser means using the 50X objective. Given a tiny focal spot to get the highest intensity means that the number of points must be increased. This, in turn, has required a major upgrade of our display system which is now in progress.

Comparing the results of the two x-ray machines gives the following:

Measurement Location	Mean Stress (ksi)	Mean Stress error (\pm ksi)
Penn State University	-133	13
Materials Technology Lab	-171	22

Summary

Thermal wave microscopy images have been used to illustrate the principles and applications of thermal wave/photoacoustic phenomena. It has been illustrated here how resolutions down to 1 μm can be attained, even on rough surfaces; how subsurface thermal structure can be imaged; how it would be possible to control laser modification of surfaces and ion implantation; and how quantification of thermal properties has begun. It is hoped that some useful ideas will have been suggested.

Acknowledgments

Many have helped in our efforts. There is only space to mention a few who were most related to what is presented here. Mr. Jim Rakowski and Mr. Milt Chaika have worked diligently to further the photoacoustic microscope and provide quantitative results. Dr. Keith Legg, now president of Ionic Atlanta, produced the data for the ion acoustic image. The thermal wave group under Profs. R. L. Thomas, L. D. Favro and P. K. Kuo provided the data for the images in Figures 2, 3, 5, and 6.

References

1. D. N. Rose, D. C. Bryk, W. D. Jackson and M. Chaika, "Resolution of Laser Generated Thermal Wave Imaging and an Example of Its Use", Proceedings of the 16th Symposium on Nondestructive Evaluation, 282-306 (1987).
2. G. H. Quay, D. N. Rose and W. D. Jackson, "One-Dimensional Single Layer Photoacoustic Theory, An Expansion of Chapter 9 of **Photoacoustics and Photoacoustic Spectroscopy** by Allan Rosencwaig", U.S. Army Tank-Automotive Command Research, Development and Engineering Center Technical Report No. 13534, Warren, MI 48397-5000, (August, 1991).
3. A. Rosencwaig, Photoacoustics and Photoacoustic Spectroscopy, John Wiley & Sons, New York (1980). A starting point for current studies.
4. H. S. Carslaw and J. C. Jaeger, Conduction of Heat in Solids, Oxford University Press, London (1959). Though 30 years old, this is the standard theoretical reference in the field.
5. G. A. West, J. J. Barrett, D. R. Siebert and K. V. Reddy, "Photoacoustic Spectroscopy", Rev. Sci. Inst., 54, 797-817 (1983). A starting point for photoacoustic spectroscopy.
6. Applied Optics, 21 (1982). The Second International Meeting on Photoacoustic Spectroscopy. This is a review of the total field at that time, not just spectroscopy.

7. Canadian Journal of Physics, 64 (1986). Proceedings of the 4th International Topical Meeting on Photoacoustics, Thermal and Related Sciences.
8. Photoacoustic and Photothermal Phenomena, Springer Series in Optical Science, P. Hess and J. Pelzl, ed., Springer Verlag, Berlin (1988). Proceedings of the 5th Topical Meeting on Photoacoustic and Photothermal Phenomena.
9. Photoacoustic and Photothermal Phenomena II, Springer Series in Optical Sciences, J. C. Murphy, J. W. MacLachlan Spicer, L. C. Aamodt and B. S. H. Royce, ed., Springer Verlag, Berlin (1990). Proceedings of the 6th International Topical Meeting.
10. C. O. Ruud and D. J. Snoha, "Investigation of Residual Stress in Structural Ceramic Components", Final Rept., US Army Contr. No. DAAG 46-83-K-0036, U.S. Army Materials Technology Laboratory, Watertown, MA 02172 (1987).
11. C. O. Ruud, D. J. Snoha and D. N. Rose, "Nondestructive Characterization of Beta Silicon Carbide CVD Coatings", Review of Progress in Quantitative Nondestructive Evaluation, 8B, 1369 - 1378, D. O. Thompson and D. E. Chimenti, ed., Plenum Press, NY, NY (1989).
12. D. J. Snoha, private communication.

DISTRIBUTION LIST

	Copies
Commander Defense Technical Information Center Bldg. 5, Cameron Station ATTN: DDAC Alexandria, VA 22304-9990	2
Manager Defense Logistics Studies Information Exchange ATRTN: AMXMC-D Fort Lee, VA 23801-6044	2
Commander U.S. Army Tank-Automotive Command ATTN: ASQNC-TAC-DIT (Technical Library) Warren, MI 48397-5000	2
Commander U.S. Army Tank-Automotive Command ATTN: AMSTA-CF Warren, MI 48397-5000	1
Director U.S. Army Materiel Systems Analysis Activity ATTN: AMXSY-MP (Mr. Cohen) Aberdeen Proving Ground, MD 21005-5071	1